Evaluating fitting models of the missing energy contribution of Ar and Ti nuclear shell orbitals using the E12-14-012 (e,e′p) scattering experiment at Jefferson Lab

Adam Dirican,[1,*] Zachary Jerzyk,[2,†] Camillo Mariani,[3,‡] and Libo Jiang[3,§]

[1] *Department of Physics, University of Maryland, College Park, MD 20742*
[2] *Department of Physics, St. Norbert College, De Pere, WI 54115*
[3] *Center for Neutrino Physics, Virginia Polytechnic and State University, Blacksburg, VA 24061*

(Dated: August 4, 2021)

The Deep Underground Neutrino Experiment (DUNE) seeks to probe CP-symmetry violation by observing the difference in oscillation rates of the neutrino and antineutrino, detect supernovae neutrinos, and potentially invalidate several grand unification theories by making the first observation of proton decay. DUNE will be one of the leading long-baseline neutrino experiment, and it will use a liquid argon time-projection chamber (LAr-TPC) style detector. However, little work has been done on electron-nucleus scattering for isospin nonsymmetric atoms, let alone neutrino-nucleus scattering for the argon-40 specific to DUNE. In the Hall A experiment E12-14-012 at Jefferson Lab, the $(e,e'p)$ scattering cross sections of argon (N=22) and titanium (Z=22) were measured against a detailed Monte Carlo (MC) simulation. Various kinematical cuts were performed on the experimental data and MC for signal identification. Using CERN's Minuit package in ROOT, minimization was performed on each orbital's cross section as a function of missing energy against either a Gaussian (symmetric) or Maxwell-Boltzmann (nonsymmetric) distribution and dependence or independence of the function on the mean energy. Goodness of fit was calculated using a χ^2 function that compared experimental data against the MC. Nuclear spectral functions provided the basis for the initial fit models of argon and titanium from which model variants were chosen. After removing poor models from analysis due to large reduced-χ^2 values or non-physical parameters, several fit models showed good agreement. We determined that the minimization process did not introduce a statistically significant systematic error due to the choice of fit models.

I. INTRODUCTION AND MOTIVATION

Neutrino physics is among the most rapidly developing sub-fields of contemporary science. Answering questions about the neutrino helps answer fundamental questions on matter-antimatter asymmetry, supernovae formation, and hypothesized grand unification theories. The Deep Underground Neutrino Experiment (DUNE) seeks to investigate all of these topics by tracking quantities of muon neutrinos and antineutrinos as they evolve into electron neutrinos and antineutrinos through a process called neutrino oscillation [1, 2].

An international experiment with facilities at Fermilab in Illinois and Sanford Underground Research Facility (SURF) in South Dakota, a sponsorship from the US Department of Energy, and collaborators from institutions around the world, DUNE is expected to be the largest baseline neutrino experiment in the world [3]. Construction will begin in 2023 and finish in 2029, with the first data run beginning shortly thereafter.

The experimental process will begin with the generation of an intense, powerful proton beam (1.0-1.2 MW, 60-120 GeV) at the Fermilab proton accelerator. To produce a neutrino beam, the proton beam will strike a target, producing a shower of positively charged pions and positively charged kaons which are directed into a tight beam by magnetic rings called "horns". These pions and kaons then decay into muons and muon neutrinos. The same process is done to create an antineutrino beam, however the pions and kaons produced are negatively charged and the horns have their fields reversed [4].

The (anti-)neutrino beam then travels through about 300 m (1000 ft) of solid earth with nearly no drop in particle flux, until it reaches the *near detector*. Effectively, the near detector should measure the muon (anti-)neutrino mass-energy spectrum.

The near detector will provide a control number of near detector events to be compared against the *far detector* (called the Underground Particle Detector in Fig. 1). The far detector will be placed roughly 1300 km from the near detector at a depth of 1450 meter-water equivalents (MWE) or about 1500 meters [6].

Both detectors will essentially be a large chamber with two opposing sides placed at opposite charge, filling the cavity with an electric field (adjustable to over 500 V/cm [7]). The cavity will be filled with liquid argon. The (anti-)neutrinos will enter the chamber, scatter off some of the liquid argon nuclei, and produce Coulombically charged products. These products will then be pulled by the electric field and hit an intricate data acquisition system (DAQ) placed along the anode side of each of the chamber. The sophistication of the DAQ will allow the the energy spectra of muon and electron (anti-)neutrinos to be reconstructed, and the oscillation probability to be measured with high accuracy.

However, no detailed model exists for how neutrinos scatter off argon-40 nuclei, introducing an unacceptably large systematic error—hence, Jefferson Laboratory's (JLab) E12-14-012 experiment. Its purpose is

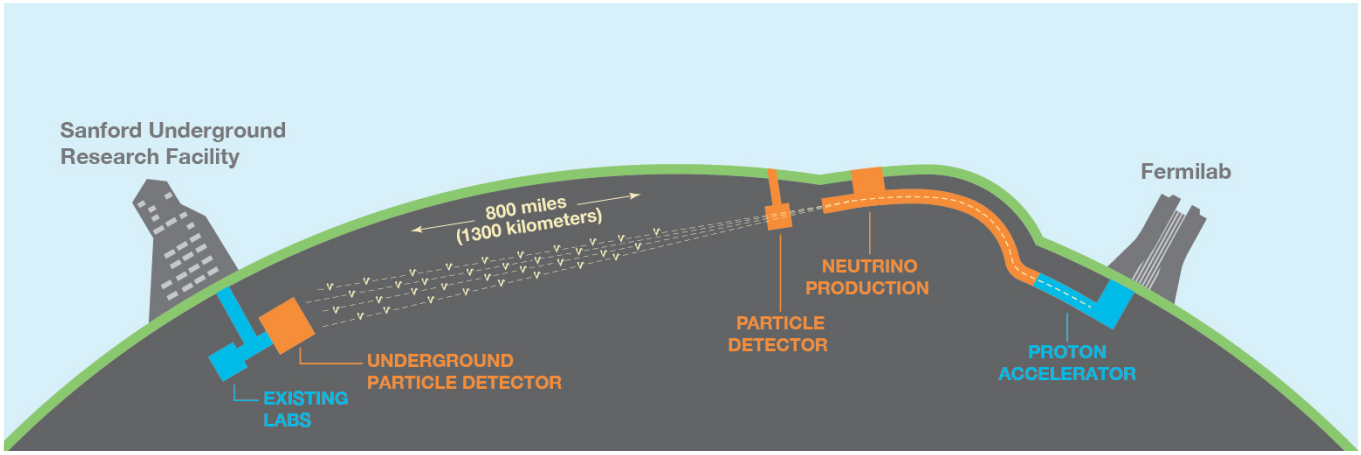

FIG. 1. The DUNE Experimental Setup. Figure from Ref. [5].

to build a reliable proton model of the argon-40 and titanium-48, which will be combined to create a total nuclear model of argon-40. The JLab experiment will have an electron beam, hit a target (either natural gaseous argon or natural solid titanium), knock free one proton, and measure the associated energies, momenta, and outgoing particle angles. Data taken by JLab is compared against a detailed Monte Carlo simulation with a set of distributions (one per proton orbital) prescribed by a set of parameters (three per orbital: maximum, mean, and standard deviation) which are varied to minimize their χ^2.

But, Monte Carlo simulations can surreptitiously introduce systematic errors if parameters are correlated to one another. Hence, such biases must be checked for. One method of doing so is to model the orbitals in various ways, using physical intuition and χ^2 testing to check results. If sufficiently many results agree with one another and physical predictions, we can say with confidence that this experimental and Monte Carlo data comparison and modeling method does not introduce systematic bias.

A. Neutrinos, antineutrinos, and neutrino oscillation

Neutrinos were first hypothesized in 1930 by Wolfgang Pauli to explain the energy distribution of electrons (or positrons) created during beta decay processes. It took until 1956 for Reines and Cowan to make the first empirical observation with a giant detection tank placed outside a nuclear reactor, looking for the products of inverse beta decay. After the discovery, they sent a telegram to Pauli: "We are happy to inform you that we have definitively detected neutrinos" [8].

Neutrinos are very light and do not have a charge. Their only distinguishing feature is that they have a small, nonzero mass. In being non-charged and nearly massless, they very rarely interact with other particles.[1]

They come in three so called *leptonic flavors*: electronic, muonic, and tauonic.[2] These three flavors are distinguished by their mass and are canonically produced by the decay of a virtual W^+ boson:

$$W^+ \longrightarrow l^+ + \nu_l \tag{1}$$

where l^+ represents any of the three positively charged leptons—e^+ for positron, μ^+ for antimuon, and τ^+ for antitauon—and ν_l represents the associated lepton flavored neutrino. And, in the decay of a virtual W^- boson, we have:

$$W^- \longrightarrow l^- + \bar{\nu}_l \tag{2}$$

where l^- are any of the three negatively charged leptons—e^- for positron, μ^- for muon, and τ^- for tauon—and $\bar{\nu}_l$ represents the associated lepton-flavored *anti*neutrino. Thus, lepton flavor is well-defined in the (anti-)neutrino. After production, as a neutrino with one flavor propagates through time, it oscillates through each of the three flavors, at some times being mostly one flavor and at others a good mix. Thus, each of the three lepton pure neutrino states form a flavor eigenbasis through which any individual neutrino oscillates as it propagates through time. This is the phenomenon of *neutrino oscillation*.

However, such "flavor pure" neutrinos are not well-defined in mass. A second 3-dimensional eigenbasis, the *mass* eigenbasis, is well-defined and thus describes

[1] Neutrinos are so non-interactive, if you were to put a flux of them through 1 light-year of lead, only half would be stopped!

[2] There is also the distinction of active and sterile neutrinos, which is beyond the scope of this document.

the mass of any flavor pure neutrino as a superposition. Then, as per the rules of linear algebra and quantum mechanics (this is a time propagating phenomenon), there ought to be a unitary matrix, call it $\mathcal{U}$, which rotates the mass eigenbasis into the flavor eigenbasis:

$$\begin{pmatrix}\nu_e\\ \nu_\mu\\ \nu_t\end{pmatrix} = \mathcal{U}\begin{pmatrix}\nu_1\\ \nu_2\\ \nu_3\end{pmatrix} \tag{3}$$

where ν_{1-3} represent the three mass eigenbases. In the literature, this matrix is called the Pontecorvo-Maki-Nagakawa-Sakata (PMNS) matrix. Adjacently in quark physics, there is a very similar object called the Cabibbo–Kobayashi–Maskawa (CKM) matrix that describes the phenomenon of *quark mixing*. The CKM describes how, much like in neutrino oscillation, quarks propagating through time oscillate through their own various quark flavors.

Moreover, in treating $\mathcal{U}$ as a basis transformation matrix, we can decompose it into three rotation matrices, each rotating some angle about a mass eigenvector. In form, they will be exactly the same as rotations about the x, y, and z axes in the cartesian coordinate system. Let us call them $\mathcal{R}_1(\theta_{23})$, $\mathcal{R}_2(\theta_{13})$, and $\mathcal{R}_3(\theta_{12})$, respectively for rotations about mass eigenvectors 1 through 3 and with fixed so-called *mixing angles* θ_{23}, θ_{13}, and θ_{12}. Thus, $\mathcal{U}$ should be something like

$$\mathcal{U} \sim \mathcal{R}_1(\theta_{23})\mathcal{R}_2(\theta_{13})\mathcal{R}_3(\theta_{12}). \tag{4}$$

However, this is not the end of the story.

B. CP violation and matter-antimatter asymmetry

The CPT theorem is one of the most fundamental in all of contemporary physics. It states that every relativistic quantum field theory has a symmetry upon simultaneous reversal of charge (C), parity (P), and time (T).[3]

However, the CPT theorem says nothing of possible symmetries in reversing any proper subset of charge, parity, and time. In fact, all of the proper subsets can have their symmetries broken. For us, our interest lies in CP-symmetry as quark mixing breaks CP-symmetry. So, it is reasonable to hypothesize that neutrino oscillation may break CP-symmetry also. If CP-symmtery is broken, we should expect that the probability of a neutrino to oscillate from one state to another should not be the same for an antineutrino, namely that

$$P(\nu_\alpha \to \nu_\beta) \neq P(\bar{\nu}_\alpha \to \bar{\nu}_\beta). \tag{5}$$

To fit such a hypothesis into our $\mathcal{U}$ matrix from the previous section, we can simply introduce a 3×1 matrix parameterized by some δ_{CP} (think of the parameter as how CP-violating neutrino oscillations is[4]) to one of the rotation matrices. Let us call the matrix $V(\delta_{CP})$, where we may define it as

$$V(\delta_{CP}) = \begin{pmatrix} e^{i\delta_{CP}} \\ 1 \\ e^{-i\delta_{CP}}\end{pmatrix}. \tag{6}$$

So, finally altogether we can say,

$$\mathcal{U} = \mathcal{R}_1(\theta_{23})\mathcal{R}_2(\theta_{13})V(\delta_{CP})\mathcal{R}_3(\theta_{12}) \tag{7}$$

$$= \begin{pmatrix}1 & 0 & 0\\ 0 & c_{23} & s_{23}\\ 0 & -s_{23} & c_{23}\end{pmatrix}\begin{pmatrix}c_{13} & 0 & s_{13}\\ 0 & 1 & 0\\ -s_{13} & 0 & c_{13}\end{pmatrix}\begin{pmatrix} e^{i\delta_{CP}} \\ 1 \\ e^{-i\delta_{CP}}\end{pmatrix}\begin{pmatrix}c_{12} & s_{12} & 0\\ -s_{12} & c_{12} & 0\\ 0 & 0 & 1\end{pmatrix} \tag{8}$$

where $c_{ij} = \cos(\theta_{ij})$, $s_{ij} = \sin(\theta_{ij})$, and the placement and specific form of $V(\delta_{CP})$ is chosen.

If we find that neutrinos do break CP-symmetry, it implies a possible course of events in the early Universe resulting in the dominance of matter over antimatter that we see today. Basically, if CP-symmetry is broken, a process called *leptogenesis* can occur, whereby more leptons are created than anti-leptons. In turn, another process takes hold called *baryogenesis*, where more baryons (e.g. electrons, neutrons, and protons) are created than anti-baryons. Thus, if $\delta_{CP} \neq n\pi, n \in \mathbb{Z}$, we have a mechanism explaining how the Universe has more matter than anti-matter. Our discussion on the subject of CP-symmetry breaking in leptons implying a matter-antimatter disparity has thus far been rather facile. More can be said on the topic, but in the interest of brevity, we suggest reading more in Ref. [9].

C. Supernovae and neutrinos

When a massive star dies in a supernova explosion, a spectacular 10^{58} neutrinos of all flavors are emitted [10]. The only neutrino burst directly detected so far has been the SN 1987A supernova analyzed by Davis and Koshiba

[3] By "charge reversal", we mean not only negating Coulombic charge, but also the charges associated with the other fundamental forces. By "parity reversal" we mean reversing one spatial dimension. And for what it means to reverse time, well, as the saying goes: time is what the clock measures.

[4] If CP-symmetry is not violated, simply have $\delta_{CP} = 0$ and recover a CP-symmetry conserving $\mathcal{U}$.

(another Nobel Prize winning pair), although many stars have gone supernova since. As the DUNE manual states: "This sample has nourished physicists and astrophysicists for many years, but has by now been thoroughly picked over. The community anticipates a much more sumptuous feast of data when the next nearby star collapses" [11].

Due to the construction of the time-projection chamber and the isospin nonsymmetry of argon-40, DUNE will be able to reconstruct the path of incoming background cosmic neutrinos, and point back at their origin in the sky for further analysis. At the moment, only Super-Kamiokande is able to do this with sufficient precision. But, once DUNE and collection of other neutrino detectors across the globe (e.g. JUNO, Hyper-Kamiokande, IceCube) are all finished and working together, with DUNE providing is particularly strong sensitivity for ν_e signals, there will be an enormous amount of data for astrophysicists to study supernovae phenomena. You can read more on the subject here: [11, p.235-260]—and here: [12].[5]

D. Hypothesized proton decay

Since the middle of the 1970s, physicists have been looking for a theory unifying the four fundamental forces of nature, so-called Grand Unified Theories (GUTs). Such GUTs predict various decay modes for the proton with associated decay lifetimes. DUNE will be able to search for many of these decay modes, particularly $p \longrightarrow K^+ + \bar{\nu}$ as the LArTPC will be very sensitive to kaon decay products.

Again, you can read more on the subject here: [11, p.210-234]. See particularly the diagram on page 211 of the PDF file for the various associated proton decay modes, GUTs, and experimental sensitivities.

II. NEUTRINO-NUCLEUS SCATTERING THEORY

A. Electron-nucleus scattering

1. Classical scattering

Imagine a billiards table. You strike a ping-pong ball at an 8-ball slightly off center, having it bounce away at some angle with negligible recoil on the 8-ball. Call the distance off center the *impact parameter* b, the outgoing angle of the ping pong ball the *scattering angle* θ, and the 8-ball radius R. The question is whether b and θ can be associated. Diagramming the scenario (see FIG. 2) and observing by simple geometry and conservation of momentum reveals that they can indeed be related.

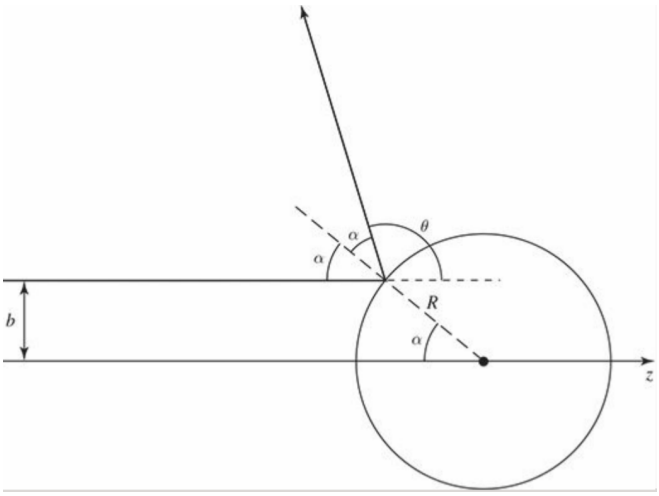

FIG. 2. A hard-sphere scattering diagram. A smaller ball approaches the larger one (of radius R) with impact parameter b and bounces off at scattering angle θ without imparting any recoil to the larger ball. This is the simplest problem in scattering theory. Figure from Ref. [13].

$$b = R\sin(\alpha) = R\sin\left(\frac{\pi-\theta}{2}\right) = R\cos\left(\frac{\theta}{2}\right). \qquad (9)$$

We have just effectively "solved" the problem of elastic hard-sphere scattering. Now, let us imagine something harder.

2. Quantum elastic scattering

Suppose an electron beam is incident on an atomic nucleus. In 3-dimensions the situation should look something like FIG. 3:

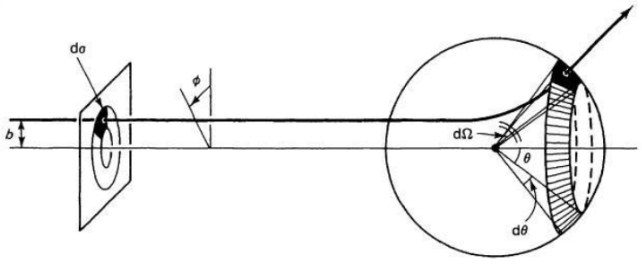

FIG. 3. "Particles incident in the area $d\sigma$ scatter into the solid angle $d\Omega$." Associating the two differentials is the main objective of scattering experiments. Quoted caption and figure from Ref. [14].

[5] Lipari's work is a particularly nice introduction to neutrino physics.

where regions on the incoming electron beam, $\Delta\sigma$, are associated to solid angles that the outgoing electrons can travel through, $\Delta\Omega$. By continuity, we can argue there ought to be a probabilistic (remember that the electron and nucleus are described by wavefunctions) function relating differentials on each surface, namely that

$$d\sigma = D(\theta)d\Omega \iff D(\theta) = \frac{d\sigma}{d\Omega}. \tag{10}$$

Finding such a $D(\theta)$ by knowing $d\sigma$ and measuring $d\Omega$ is the central motive of scattering experiments. This proportionality factor is called the *differential cross section*[6] of the scattering.

Moreover, note that this kind of collision (i.e. electron scatters off nucleus but does not knock free any protons) is denoted as an "(e,e') scattering".

3. Electron-proton scattering

Finally, let us examine one further case still, the $(e,e'p)$ scattering, where an electron knocks free one proton from the target nucleus. Assume that before the collision, the target nucleus is more or less at rest (you can cool the target; plus random kinetic motion of target nuclei are omni-directional, so the effect ought to cancel over many trials).

Given that now this scattering scenario involves intranuclear interactions with sufficient energy to free protons, we must give the problem a quantum field theory (QFT) treatment, as well as consider the collision as inelastic. Appealing to QFT, let us imagine that the electron exchanges (for simplicity) exactly one virtual photon (of energy $\hbar\omega$ and momentum $\boldsymbol{q}$) with the target nucleus. And, to account for the inelasticity, let us also consider the recoil energy and momentum of the recoiling nucleus, labeling them T_{A-1} and $\boldsymbol{P}_{A-1}$, respectively.

Knowing ahead of time the kinetic energy T_e and momentum $\boldsymbol{p}_e$ of the incoming electron, holding the emission angles constant (over many trials), and measuring after collision the outgoing electron and proton's kinetic energies $T_{e'}$ and T_p, and momenta $\boldsymbol{p}_{e'}$ and $\boldsymbol{p}_p$, we collect as much data external to the electron-nucleus interaction as possible.

However, what we cannot account for are the internals of the nucleus, within which the incoming electron can deposit some energy and momentum. These are called the *missing* energy and *missing* momentum. Let us denote them E_m and $\boldsymbol{p}_m$, respectively. The missing energy is the difference between the photon energy and the energy the proton and nucleus take on:

$$E_m = \hbar\omega - T_p - T_{A-1}. \tag{11}$$

Then, applying momentum conservation, we can compute the missing momentum distribution for the whole recoiling nucleus. So, the missing momentum is

$$\boldsymbol{p}_m = \boldsymbol{q} - \boldsymbol{p}_p = \boldsymbol{P}_{A-1}. \tag{12}$$

Again, a relation between $d\sigma$ and $d\Omega$, like $D(\theta)$ from the previous problem, is our interest. Here we define our relation as the *double differential cross section*:

$$\mathcal{D} \equiv \frac{d^6\sigma}{d\omega d\Omega_{e'} dT_p d\Omega_p} \tag{13}$$

where both solid angles are variables of two dimensions. The general theory states that in these $(e,e'p)$ scatterings the double differential cross section is proportional to the outgoing proton *spectral function*. Let us call it $\mathcal{P}$, and note that it is a function of the missing energy and momentum. To scale correctly, the proton spectral function must be multiplied by the proton energy E_p, momentum vector magnitude $|\boldsymbol{p}_p|$, and the cross section for an electron to hit any one bound proton in the nucleus, which we will call σ_{ep}. Thus, altogether we have

$$\boxed{\mathcal{D} \equiv \frac{d^6\sigma}{d\omega d\Omega_{e'} dT_p d\Omega_p} = |\boldsymbol{p}_p| E_p \sigma_{ep} \mathcal{P}(E_m, \boldsymbol{p_m})} \tag{14}$$

which forms the basic theory of our measurements from the $(e,e'p)$ scattering experiment at JLab.

B. Electron-nucleon scattering vs. neutrino-nucleon scattering

The goal of the JLab E2-14-012 experiment is to model neutrino-nucleus scattering in argon-40 for DUNE.

Under two basic assumptions—scattering involves only individual nucleons and the outgoing proton does not interact at all with the other *spectator* nucleons—we may connect the proton spectral function for electron-proton scattering to a nucleon spectral function for neutrino-nucleon scattering. We use a mathematical object called a *Gorkov self-consistent Green function*, or *nucleon Green function* in our case, for short. This is a concept from Bardeen-Cooper-Schrieffer (BCS) superconductivity theory.

Effectively, we enforce a "grand-canonical" potential which only has the correct number of protons and neutrons *on average*. Thus, off-shell activity in the nucleus

[6] The name *differential cross section* can be quite misleading, as $D(\theta)$ is neither a differential nor a cross section. To quote David Griffiths on the term: "This is terrible language...[b]ut I'm afraid we're stuck with this terminology."

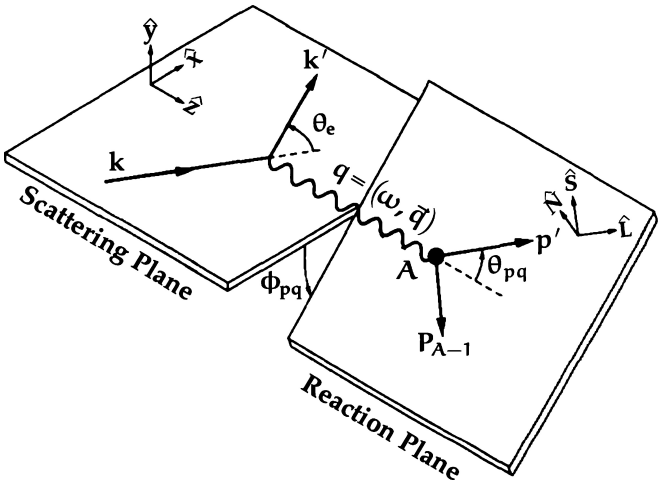

FIG. 4. Kinematics of the incoming electron e with its associated wavevector, $\boldsymbol{k}$, the outgoing electron e' with wavevector $\boldsymbol{k}'$, the outgoing proton p with momentum vector $\boldsymbol{p}$, and recoiling proton-decremented nucleus denoted P_{A-1}. Note that the electron and nuclear planes (at the moment of contact, indicated by the two vertices) exchange a virtual photon, q, with associated frequency ω and momentum transfer vector $\vec{q}$. Finally, observe that each of the two scattering products has an corresponding angle, namely θ_e for e' and θ_{pq} for p, as well as an azimuthal angle between the planes, ϕ_{pq}. Figure from Ref. [15].

can be considered[7] Ultimately, the proton spectral function for electron scattering is related to the Green function of the nucleon spectral function for neutrino scattering, call it G, by the following equivalence:

$$\mathcal{P}(\boldsymbol{p}_p, E_p) = \frac{1}{\pi}\mathrm{Im}[G(\boldsymbol{p}_p, E_p)] \tag{15}$$

where both functions are dependent on the outgoing proton's momentum and energy. Thus, in measuring the proton spectral function for argon-40 and titanium-48, both can be converted into nucleon spectral functions ($N = 22$ for argon and $Z = 22$ for titanium) and combined for the full nucleon spectral function in neutrino-nucleus scattering for argon-40 [17].

C. Liquid argon time projection chambers

A time projection chamber (TPC) is a specialized type of particle detector featuring a volume of fluid medium contained within electromagnetic fields intended to three-dimensionally reconstruct the trajectory of particles as they undergo reaction within the detection chamber [18].

[7] Again, getting deeply into the subject will take us too far off course for this paper So, we leave you another couple of sources to examine for yourself if you are so interested: [16, 17].

Originally designed and invented by David Nygren in the 1970s, the TPC was intended to address the need for better momenta construction and identification of high energy charged particles, essential to experimental particle physics [19]. The advantages of the design as Nygren proposed were the ability to reconstruct particle interactions in space and time and the high resolution of both the spatial and time reconstructions. He also noted the simplicity of the detector's main component being a gaseous volume, the increase in efficacy with higher magnetic fields, and the general independence of the detector's orientation preferences—reconstruction is about equally achievable for any path taken by an incoming particle [20].

1. TPC design

A standard TPC is constructed as a volume of fluid medium enclosed between a cathode and an anode plane which induce an electric field, causing electrons, resulting from ionization due to energetic particle collision, to drift. This can be seen as somewhat analogous to a large capacitor plate construction with a fluid dielectric.[8] A magnet is placed such that its magnetic field lines run uniformly parallel with the electric field lines, eliminating the $E \times B$ forces otherwise imparted on the ionization electrons and allowing for sizable electron drift distances, aiding in event reconstruction [18].

The early TPC models[21] have since been revised to favor using liquid argon as a medium over a gaseous medium, and so are named "liquid argon time projection chambers" (LAr-TPCs). In this design, (anti-)neutrinos travel between the cathode and anode, scattering off argon nuclei along the path. The products of these interactions then reach the anode and are measured using an intricate data acquisition system (DAQ).

[8] Note however that this is just analogy about the parts of the TPC. The TPC medium is not intended to be a good dielectric.

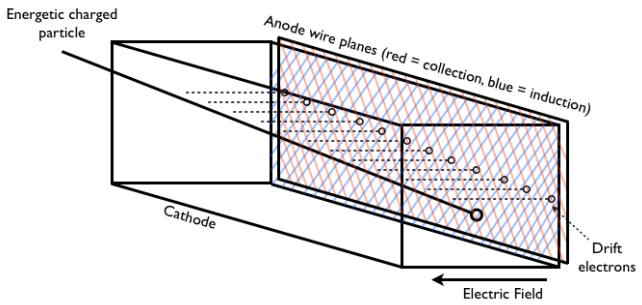

FIG. 5. A simplification of the time projection chamber style detector that will be used at DUNE. (Anti-)neutrinos travel through the liquid argon medium, producing excited electrons whose arrival at the anode plane can be used to reconstruct the (anti-)neutrino energy spectrum. Figure from Ref. [22].

Several characteristics of argon contribute to its present status as the best medium for a TPC [23]. It is very dense in its liquid state, about 40% more so than water, increasing the chances of neutrino interaction. As a noble element, argon also has a negligibly small electronegativity, allowing for easy ionization due to interaction on the order of $55,000\ e^-/cm$ [24]. If the argon is of a high enough purity—and Argon is easily purified—electrons produced in interaction will not join with the inert argon atoms, nor will they be absorbed by contaminants such as oxygen and water, allowing for high electron lifetimes and long drift periods in the chamber [25]. Argon produces considerable amounts of scintillation light ($40,000\ \gamma/MeV$), caused by the release of scintillation photons when an energetic particle passes through and deposits energy in the argon [26]. Argon is also transparent, making scintillation light detection simpler. Detecting scintillation light is useful since information about energy deposited in the argon during interaction allows for accurate reconstruction of the energies and events of the incident particles interacting in the chamber [24]. Aside from the variety of technical advantages liquid argon has for TPC construction, it is abundant in the atmosphere ($\approx 1\%$) and thus easily accessible and cheaply available (\$2/L). The main drawback of using liquid argon as a medium comes from the cost of maintaining a cryogenic environment, though argon is relatively easily liquefied using liquid nitrogen [23].

2. The DUNE LAr-TPC

To be located deep underground (about 1500 m) [1] within a South Dakota mine at SURF, the single phase LAr-TPC installation that will be featured in the DUNE uses four distinct chambers separated by alternating cathode and anode plane assembly dividers (shown in FIG. 6), where the so-called "anode plane assembly" (APA) (shown in FIG. 7) is composed of three sets of

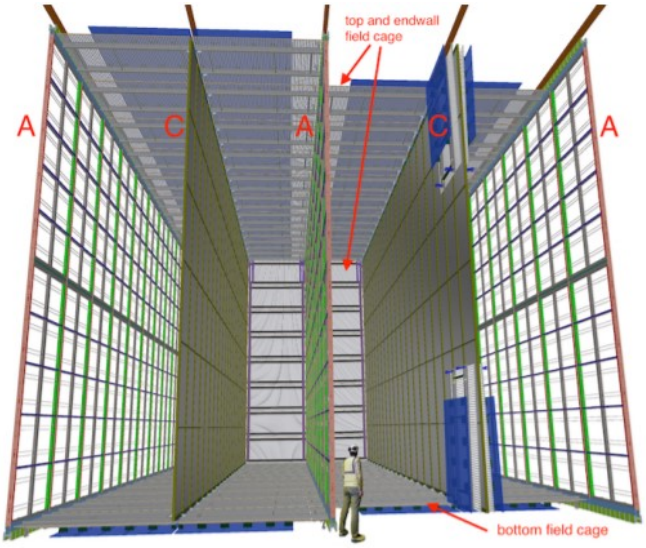

FIG. 6. "A 10 kt DUNE FD SP module, showing the alternating 58.2 m long (into the page), 12.0 m high anode (A) and cathode (C) planes, as well as the field cage (FC) that surrounds the drift regions between the anode and cathode planes. On the right-hand cathode plane, the foremost portion of the FC is shown in its undeployed (folded) state." Caption and figure from Ref. [25].

wires arranged at different angles that separately make the collection and induction planes [25]. Three of these chambers will perform LAr-TPC detecion as normal, and the last will be reserved as a module of opportunity for currently undecided future applications.

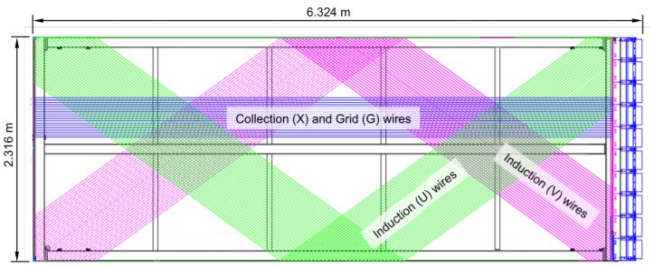

FIG. 7. "Illustration of the DUNE APA wire wrapping scheme showing small portions of the wires from the three signal planes (U,V,X). The fourth wire plane (G) above these three, and parallel to X, is present to improve the pulse shape on the U plane signals. The TPC electronics boxes, shown in blue on the right, mount directly to the frame and process signals from both the collection and induction channels. The APA is shown turned on its side in a horizontal orientation." Caption and figure from Ref. [25].

The neutrino beam, coupled with the near detector, will be located at Fermilab in Illinois, 1,300km from the DUNE LAr-TPC far detector. As the far detector will be sufficiently deep underground, superfluous cosmic particle interference will be minimized, and the weakly interacting neutrinos will be essentially unimpeded in

their travels through the earth. Calibration concerns surrounding particle energies give rise to the need for data from preceding LAr-TPC experiments in order to confidently identify various particles, which is precisely the purpose of the *Proto*DUNE LAr-TPC as prototype for the future DUNE far detector installation.

3. ProtoDUNE

The ProtoDUNE LAr-TPC is installed in the CERN's Neutrino Platform. A beam that delivers charged pions, kaons, protons, muons, and electrons for the purpose of providing beam interactions and to characterize how the DUNE detector will be able to identify these particles as well as reconstruct momenta and energies of such incident particles. Among the data that has been collected thus far with the ProtoDUNE detector, background noise for both the chamber and photon detectors has been evaluated, gain measurements made, particle energy calibrations achieved, electron lifetimes measured, and signal sensitivity and time resolution determined—all at or exceeding the standards of the specifications desired for the actual DUNE LAr-TPC [27]. In spite of these successes, the program could be furthered still by the improvement of nuclear models of the argon atom which neutrinos will evidently be scattering off of in the detector. This is the motivation for a series of nuclear-particle physics collaborative experiments performed to that end, especially ours at JLab.

III. THE JLAB EXPERIMENT ON $^{40}_{18}$Ar AND $^{48}_{22}$Ti

Data were collected in 2017 at Hall A of Jefferson Lab during Experiment E12-14-012 in 2017. Data for five kinematic configurations was taken for argon [28], and four for titanium[29]. Ten configurations were initially planned for each[30], but time and expense constraints limited the collection to five, as sufficient data was still possible with this limitation. Beyond that, the titanium data only had three complete kinematic data sets and a fraction of the fourth. Alongside the experimental data, an MC simulation was created to decompose the total nuclear spectral functions into their individual orbital contributions. The MC also allowed for a rigorous error analysis to be performed.

The experimental method was similar to the method originally used for the experiment published in 1974 regarding quasi-free (e, e′p) scattering on $^{12}_{6}$C and other elements [31]. An electron beam incident on gaseous argon-40 and solid titanium-48 targets produced these interactions at JLab, and spectrometers detected the final state electrons and protons. An apparent violation of energy and momentum is observed when comparing the known statistics of the electron beam with the statistics of the detected final state products, leading to the conclusion that final state interactions as the products exit the nucleus contribute to the losses. The missing energy and momenta are reconstructed in a distribution, and nuclear theory[32] provides the basis for which nuclear shell orbitals are expected to contribute to the overall losses. These orbital contributions are quantified as spectroscopic factors, and it is these spectral functions that are necessary in improving the model for neutrino-nucleus scattering.

Additionally, data was taken for aluminum and carbon solid targets for the same beam energy, angle, and kinematics [34]. Carbon and aluminum have comparatively simple and non-similar nuclei structures to argon and titanium, so knowledge of the nuclear effects on neutrino interaction for those elements does not meaningfully contribute to advancing future DUNE goals with LAr-TPCs, however, the motivation for taking data on these two atoms is to serve as a cross check on the data collection and analysis methods, since earlier experiments[35] have well characterized nuclear shell orbital contributions of carbon and aluminum nuclei in electron scattering. Obtaining good agreement among experiments for previously studied atoms strengthens our confidence that the argon and titanium analyses are well founded. Indeed, good agreement was found with the previous experiments from the results published from the data collected at JLab [34].

IV. REU STUDENT CONTRIBUTION

A. Motivation

In June and July of 2021, further analysis was conducted on the argon and titanium missing energy fits as a part of Virginia Tech's summer REU program. This analysis was motivated by the desire for a more complete picture of the systematic errors contributing to the goodness of fit, specifically whether or not there was a meaningful systematic error to be accounted for in the choice of how to model the nuclear shell orbital contributions in the total missing energy distribution when using both experimental and MC data. A framework for choosing relevant models to test was agreed upon, and a modular ROOT code developed to incorporate the framework and new analysis.

B. The setup

Both of the existing argon and titanium missing energy analyses prior to REU contributions featured a setup in which the orbitals could be fitted with either a completely Gaussian (symmetric) model or a hybrid model of

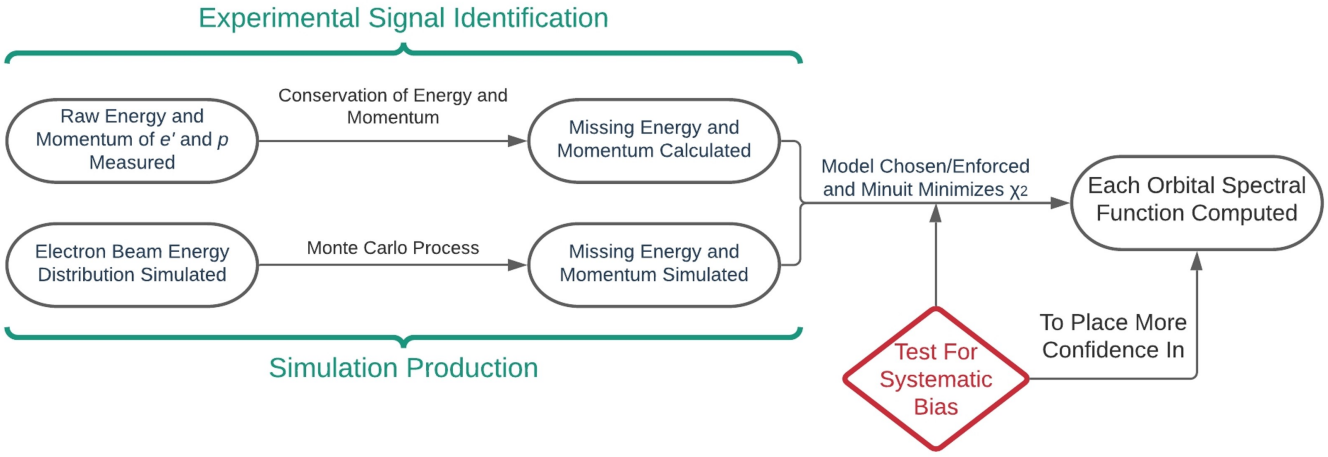

FIG. 8. Schematic of the JLab experiment, analysis, and author contribution (red). Experimental and MC data are compared against various theoretical models which may introduce a systematic bias.

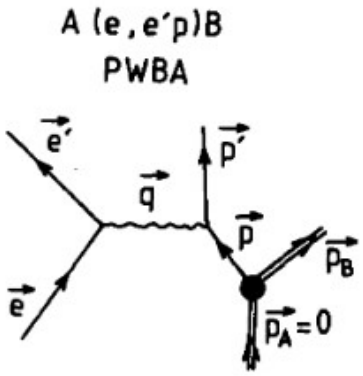

FIG. 9. "The quasi-free (e,e′p) process in Plane Wave Impulse Approximation (PWIA)." Caption and figure from Ref. [33].

Maxwell-Boltzmann (asymmetric) and Gaussian distributions. The choice between the two models was decided, orbital by orbital, based upon nuclear theory constraints, foremost the proximity of the orbital to the Fermi surface. Roughly it should be that the "closer" the distribution to the Fermi surface, the more asymmetrical such orbitals should be.

Lower energy orbitals such as the $2s_{1/2}$ and $1d_{3/2}$ orbitals are closer to the Fermi surface and thus likely to be better modeled a Maxwell-Boltzmann distribution (see FIG. 10). The initial fitting models used for argon and titanium from which the REU contributions were based are given in Tables I and II.

A goal of the REU project was to substitute the system using two distinct fitting models with a system allowing for the models of relevant groupings of orbitals to be easily changed. This was accomplished by developing a framework in which each of the nuclear shell orbitals could be modeled individually as desired, where the choice could be made between a Maxwell-Boltzmann fit or a Gaussian fit, as well as between the dependence or independence of the cross section from the mean missing energy value. With this system in place, the analysis could progress by imposing a selection of new fitting models upon the argon and titanium analyses, based on the initial fitting models. The results of these selections of new models as indicated by the reduced-χ^2 and spectroscopic factors would determine whether a systematic error would need to be imposed using a $\delta-\chi^2$ minimization technique. The table of fitting models and corresponding χ^2 results for the 17 variations of the argon analys and for the 15 variations of the titanium analysis is given in FIG. 11.

C. The Code

The fitting was performed in ROOT using the Minuit package [37], a function minimization and error analysis tool developed by and for CERN experimental nuclear physicists. Both the MIGRAD and SIMPLEX minimization algorithms were used, tools in-built in ROOT. For the minimization, the spectroscopic factor of each orbital spectral distribution (i.e. distribution maximum), its mean, and its standard deviation were assigned to a parameter value, ranging from [0]-[20] for argon and [0]-[23] for titanium. These are given for argon in Table I and for titanium in table II, both in the first modeling scheme (i.e. Model Index 1) given in FIG. 11. Graphs of all parameter values for all modeling variations (with suppression of unphysical variations) are given in the Appendix.

The code was developed for modularity, allowing it to function for both argon and titanium, and principally for other modeling analyses like this one. Designed with a

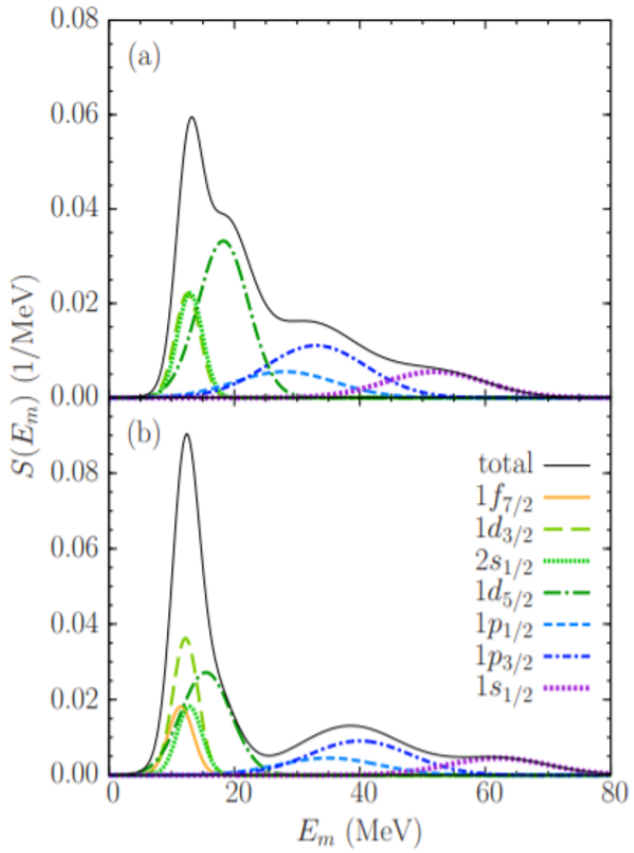

FIG. 10. Missing energy distribution of proton orbitals in (a) argon and (b) titanium. The innermost orbitals required an asymmetrical model since the distribution is increasingly asymmetric as orbitals are further from the nuclear surface. See that imposing some region of missing energy below which no orbital distribution can be due to the Fermi surface requires inner orbitals to become asymmetric. Figure from Ref. [36].

Argon					
Orbital	Energy (MeV)	Value	Mean	STD	Initial model
2s½	8	1.06	12.941	1.040	Max-Boltz; Dep.
1d⅜	6	0.760	12.524	0.639	Max-Boltz; Dep.
1d⅝	11	0.473	18.240	12.000	Max-Boltz; Dep.
1p½	28	1.024	20.638	2.482	Gauss; Indep.
1p⅜	32	0.992	32.702	5.496	Gauss; Indep.
1s½	52	1.084	52.430	11.562	Gauss; Indep.

TABLE I. Ar fitting parameter statistics for Model Index 1 (see FIG. 11). Orbital separation energies of the argon-48 proton shell model states are cited from the original proposal [30] of the E12-14-012 experiment as they were adapted from a theoretical paper by A. Ankowski [32].

high degree of customization and suppression of output, various settings can be modified in the header of the file, and logic tables work to produce the fit and graphing as desired. These are shown in the code header presented in FIG. 12.

Titanium					
Orbital	Energy (MeV)	Value	Mean	STD	Initial model
2s½	13.15	1.020	12.807	[9]	Gauss; Dep.
1d⅜	11.45	0.994	12.398	5.403	Gauss; Dep.
1d⅝	18	0.251	15.467	1.877	Gauss; Indep.
1p½	35	0.488	32.211	2.169	Gauss; Indep.
1p⅜	40	1.082	38.141	5.815	Gauss; Indep.
1s½	62	1.114	54.141	11.153	Gauss; Indep.
1f⅞	5.56	0.000	11.310	1.000	Gauss; Dep.

TABLE II. Ti fitting parameter statistics for Model Index 1 (see FIG. 11). Orbital separation energies of the titanium-48 proton shell model states are given as the argon-40 neutron shell model states, and are cited from the original proposal[30] of the E12-14-012 experiment as they were adapted from a theoretical paper by A. Ankowski [32].

V. RESULTS AND CONCLUSIONS

After assessing the various models and eliminating those that produced unphysical parameters or large reducedχ^2 values, we determined that the inter-model agreement between parameters did not require the introduction of a systematic error in either argon-40 or titanium-48. If we had found large variations in the reduced-χ^2values, or in any of the calculated parameters, we would have implemented a more sophisticated $\delta - \chi^2$ test to determine systematic biases. However, no such adjustments were necessary, and much greater confidence can be placed in the method for calculation of the spectroscopic factors in argon-40 and titanium-48.

A. Argon

Agreement among models was especially well demonstrated in argon, as the only models that were rejected (FIG. 11) were those in which the three lowest energy orbitals were fitted with a Gaussian distribution dependent on the mean energy. Further, these rejected models all had especially high reduced-χ^2 values compared to the accepted models (FIG. 13), indicating that the rejected models were simply incompatible with the fitting analysis—the fact that all other tested models showed promise allows us to place great confidence in the method for determining the spectral functions of the argon-40 protons.

B. Titanium

The reduced-χ^2 values in the titanium analysis (FIG. 14) demonstrate a much greater spread than in argon, which had values that were generally very high or very

		Argon Model Index (File #)												Additional Variations				
		1	2	3	4	5	6	7	8	9	10	11	12	13	14	15	16	17
Orbital	1d3/2, 2s1/2	MD	MD	MI	MI	MD	MD	MI	MI	GD	GD	GI	GI	MD	MD	MD	MD	MD
	1d5/2	MD	MD	MI	MI	GD	GD	GI	GI	GD	GD	GI	GI	MD	MD	MD	GI	GI
	1p1/2, 1p3/2, 1s1/2	GI	GD	GD	GI	GI	GD	GD	GI	GI	GD	GD	GI	GI	GI	GI	GI	GD
Reduced Chi-Squared		1.106	6.586	6.153	1.321	1.106	6.553	5.070	1.350	1.101	6.827	4.880	1.130	0.661	1.008	0.540	1.356	4.894

Legend			
1st Character	G	Model with Gaussian	
	M	Model with Maxwell Boltzmann	
2nd Character	D	σ is dependent on the mean	
	I	σ is independent of the mean	

		Titanium Model Index (File #)												Additional Variations		
		1	2	3	4	5	6	7	8	9	10	11	12	13	14	15
Orbital	1f7/2, 1d3/2	GD	GD	GI	GI	MD	MD	MI	MI	MD	MD	MI	MI	GD	GD	GD
	2s1/2	GD	GD	GI	GI	GD	GD	GI	GI	MD	MD	MI	MI	GD	GD	GD
	1d5/2, 1p1/2, 1p3/2, 1s1/2	GI	GD	GD	GI	GI	GD	GD	GI	GI	GD	GD	GI	GI	GI	GI
Reduced Chi-Squared		1.304	3.891	4.876	2.315	1.359	3.821	6.738	2.295	2.067	3.750	6.579	2.866	1.109	1.304	1.109

Additional Variations	
13	pm fitting results not used
14	Energy level penalty function not used
15	Neither is used

FIG. 11. The final selection of tested spectral function models for each orbital in argon (top) and titanium (bottom). Rejected models are highlighted in red according to χ^2 results, and the rightmost columns indicate additional models that were decided upon to provide a more complete analysis of the experiment-MC data comparison process.

```
/*
Legend: First array value corresponds to orbital groups:
1 --> orbital parameters 0 and 1 (2s1/2 and 1d3/2)
2 --> orbital parameter 2 (1d5/2),
3 --> orbital parameter 3 (1p1/2 and 1p3/2)
4 -- > orbital parameter 4 (1s1/2)

Second array value corresponds to two modeling choices:
        1) Gaussian (0) or Maxwell-Boltzmann (1) modeling
        2) Sigma dependece (0) or independence (1) on the mean field
both with associated booleans.

*/

int settings[4][2] = { {1,1} , {1,1} , {0,1} , {0,1}};
bool use_pm_fit_results = true;
bool use_energy_penalty_function = true;


bool CreateNewRunFile = false;
bool CreateGraphs = true;
bool SuppressSomeRuns = true;
vector <int> suppressedRuns = {2,3,6,7,10,11,12};
bool MakeLegend = true;

//Beginning of Adam and Zack's Contributions
#ifndef GLOBAL_VARIABLES
#define GLOBAL_VARIABLES
extern const string filesNameExtension = "runFile_v18-";
#endif
```

FIG. 12. Snapshot of the code header. Graphing and modeling options are contained as Booleans or 2D array entries. Note that the "settings" array being size 4×2 as opposed to 3×2 is an artifact of us having previously had 4 groups of orbitals for modeling. We found that reducing the number of groups that were modeled the same to 3 had negligible affect on our reduced-χ^2 values.

low based on consistent model criteria. No clear criteria indicated which models were appropriate for titanium. This indicates that further developments need to be made on the titanium fit analysis, and as a result we are less at liberty to place complete confidence in the determi-

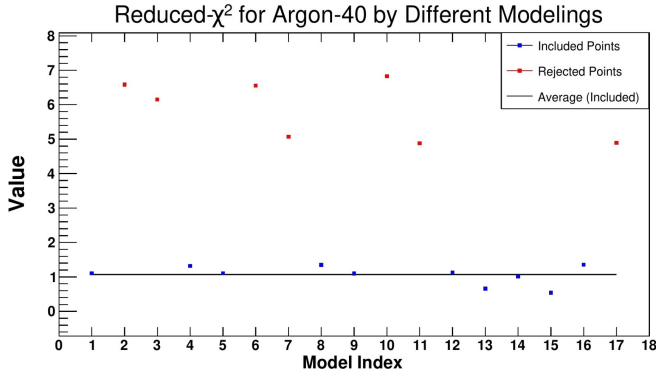

FIG. 13. Spread of reduced-χ^2 values for argon-40 corresponding to the 17 fitting models given in FIG. 11. The average bar does not account for the rejected points (red).

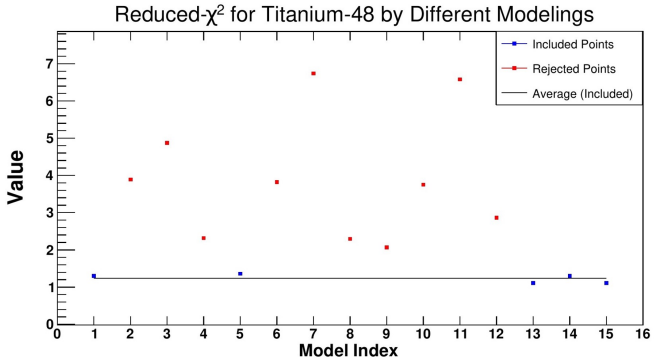

FIG. 14. Spread of reduced-χ^2 values for titanium-48 corresponding to the 15 fitting models given in FIG. 11. The average bar does not account for the rejected points (red).

nation of titanium's proton spectral functions. However, we determined that the five accepted models still provide enough consistency in the results that no systematic error would be necessary to account for choice of fit. This decision is also informed by the expectation that, once the titanium fit has developed further, the reduced-χ^2 values will ubiquitously decrease closer to unity. This expectation allows us to consider models with a value around two as potentially supportive of the quality of the titanium analysis as well.

Due to being developed first, the argon-40 data from JLab has more theoretical and computational development than the titanium-48 data. Titanium-48 also had less data taken overall and a less isotopically pure target. Moreover, extra parameters in titanium-48 meaning fitting will be a bit harder regardless of other considerations.

Future work with the JLab experiment focuses on achieving the same progress with the titanium minimization, refining our model of argon's neutron spectral functions. When the argon-40 neutrino-nucleus scattering is fully realized, far greater accuracy can be placed in Lar-TPCs like DUNE, and physics beyond the Standard Model can be fully investigated.

ACKNOWLEDGEMENTS

We thank the Virginia Tech Center for Neutrino Physics for offering this REU program, Prof. Camillo Mariani for his attentive mentorship, and finally the National Science Foundation for sponsoring this research with the NSF Grant #1757087.

* adirican@terpmail.umd.edu
† zack.jerzyk@snc.edu
‡ camillo@vt.edu
§ jiangl@vt.edu

[1] B. Abi, *et al.* (The DUNE Collaboration), Journal of Instrumentation **15**, T08008 (2020), publisher: IOP Publishing.
[2] https://www.dunescience.org/ .
[3] "Dune at lbnf," .
[4] U. Dore, P. Loverre, and L. Ludovici, The European Physical Journal H **44**, 271–305 (2019).
[5] "Home," (2021).
[6] "Detectors and computing," (2021).
[7] B. A. *et al.*, Journal of Instrumentation **15**, T08008 (2020).
[8] "History of the neutrino," (2021).
[9] M. Fukugita and T. Yanagida, Physics Letters B **174**, 45 (1986).
[10] G. Martínez-Pinedo, T. Fischer, K. Langanke, A. Lohs, A. Sieverding, and M.-R. Wu, "Neutrinos and Their Impact on Core-Collapse Supernova Nucleosynthesis," in *Handbook of Supernovae*, edited by A. W. Alsabti and P. Murdin (2017) p. 1805.
[11] t. B. Abi, "Deep underground neutrino experiment (dune), far detector technical design report, volume ii: Dune physics," (2020), arXiv:2002.03005 [hep-ex].
[12] P. Lipari, in *1st CERN-CLAF School of High-Energy Physics* (2001).
[13] D. J. Griffiths and D. F. Schroeter, "Scattering," in *Introduction to quantum mechanics* (Cambridge University Press, 2018) p. 475–509, 2nd ed.
[14] D. J. Griffiths, "Scattering," in *Introduction to quantum mechanics* (Pearson Education, 2005) p. 394–419, 2nd ed.
[15] T. Kolar, *et al.*, Physics Letters B **811**, 135903 (2020).
[16] F. Altomare and A. M. Chang, "Part one: Theoretical aspects of superconductivity in 1d nanowires," in *One-dimensional superconductivity in nanowires* (Wiley-VCH-Verl, 2013) p. 3–26.
[17] C. Barbieri, N. Rocco, and V. Somà, Phys. Rev. C **100**, 062501 (2019).
[18] J. Marx and D. Nygren, Physics Today **31** (1978), 10.1063/1.2994775.
[19] D. Nygren, PEP **144**.
[20] D. Nygren, LBL internal report (1974).
[21] R. Bouclier, G. Charpak, Z. Dimčovski, G. Fischer, F. Sauli, G. Coignet, and G. Flügge, Nuclear Instruments and Methods **88**, 149 (1970).
[22] Rlinehan, "Real schematic tpc," (2015), file: RealSchematicTPC.png.
[23] C. Rubbia, European Organization for Nuclear Research Internal Reports **77-8**, 1 (1977).
[24] J. Asaadi, "Liquid argon time projection chambers,".
[25] B. Abi, *et al.* (The DUNE Collaboration), Journal of Instrumentation **15**, T08010 (2020), publisher: IOP Publishing.
[26] C. Mariani, "Neutrinos... an interesting journey," (2021).
[27] B. Abi, *et al.*, Journal of Instrumentation **15**, P12004 (2020).
[28] H. Dai, *et al.* (The Jefferson Lab Hall A Collaboration), Phys. Rev. C **99**, 054608 (2019).
[29] H. Dai, *et al.* (Jefferson Lab Hall A Collaboration), Phys. Rev. C **98**, 014617 (2018).
[30] A. Ankowski, *et al.*, arXiv:1406.4080 [nucl-ex, physics:nucl-th] (2014), arXiv: 1406.4080.
[31] J. Mougey, M. Bernheim, A. Bussière, A. Gillebert, Phan Xuan Hô, M. Priou, D. Royer, I. Sick, and G. Wagner, Nuclear Physics A **262**, 461 (1976).
[32] A. M. Ankowski and J. T. Sobczyk, Phys. Rev. C **77**, 044311 (2008).
[33] J. Mougey, Nuclear Physics A **335**, 35 (1980).
[34] M. Murphy, *et al.* (The Jefferson Lab Hall A Collaboration), Physical Review C **100**, 054606 (2019).
[35] U. Amaldi, G. C. Venuti, G. Cortellessa, C. Fronterotta, A. Reale, P. Salvadori, and P. Hillman, Physical Review Letters **13**, 341 (1964).
[36] L. Gu, D. Abrams, A. M. Ankowski, L. Jiang, B. Aljawrneh, S. Alsalmi, J. Bane, A. Batz, S. Barcus, M. Barroso, and et al. (The Jefferson Lab Hall A Collaboration), Physical Review C **103**, 034604 (2021).
[37] F. James, *MINUIT Function Minimization and Error Analysis: Reference Manual Version 94.1*, CERN, Geneva, Switzerland (1994).

APPENDIX

The appendix contains the graphs of all model indices for argon and titanium for all distribution parameters. Legend: Included models are shown in blue and rejected in red. The average of the included models is shown as a **black line**, with the error propagated by quadrature in yellow.

ARGON

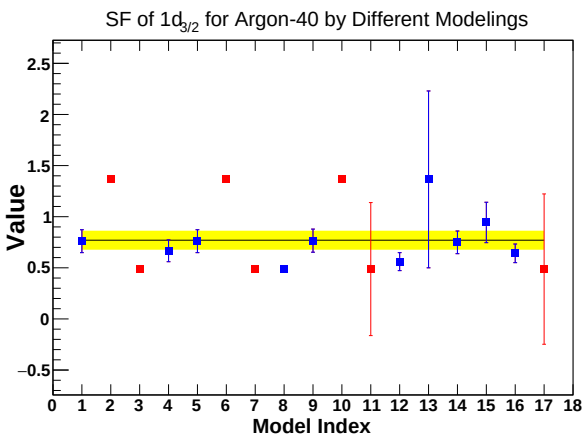
SF of 1d3/2 for Argon-40 by Different Modelings
Value
Model Index

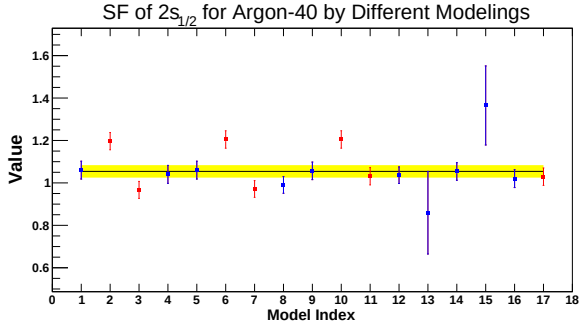
SF of 2s1/2 for Argon-40 by Different Modelings
Value
Model Index

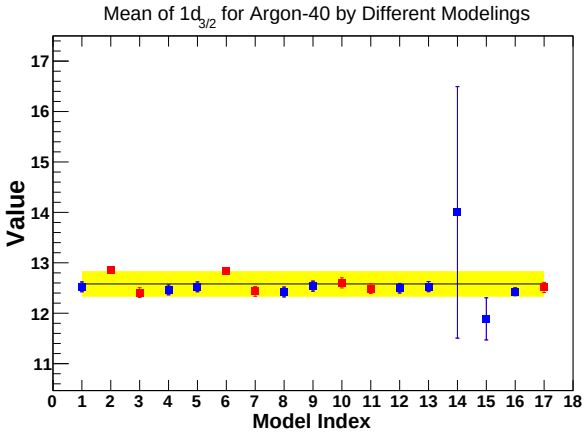
Mean of 1d3/2 for Argon-40 by Different Modelings
Value
Model Index

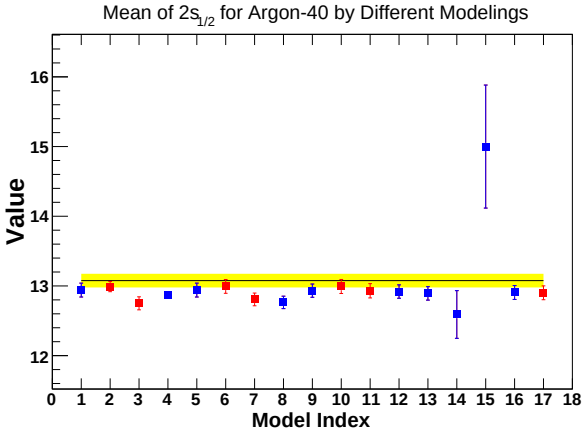
Mean of 2s1/2 for Argon-40 by Different Modelings
Value
Model Index

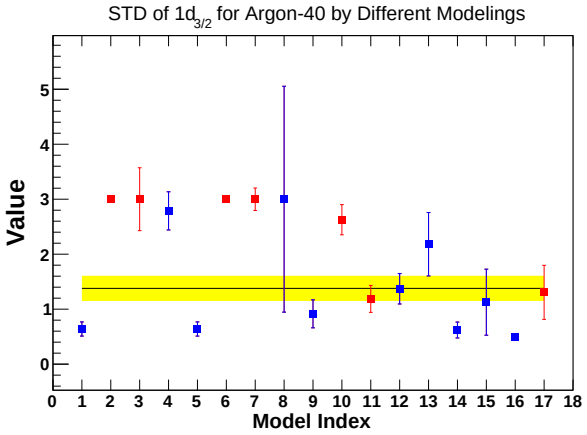
STD of 1d3/2 for Argon-40 by Different Modelings
Value
Model Index

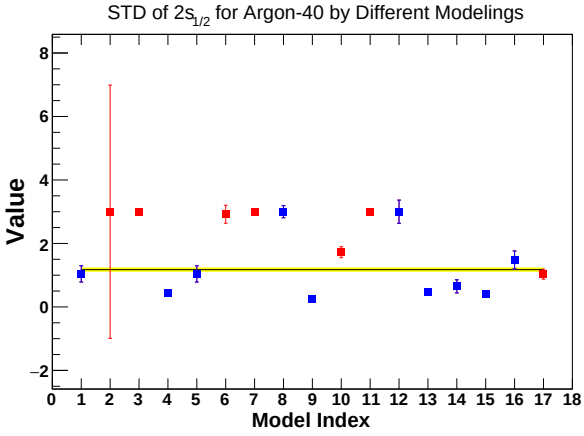
STD of 2s1/2 for Argon-40 by Different Modelings
Value
Model Index

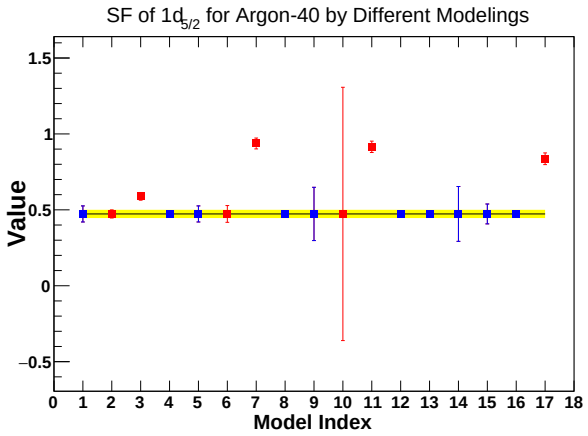
SF of 1d5/2 for Argon-40 by Different Modelings
Value
Model Index

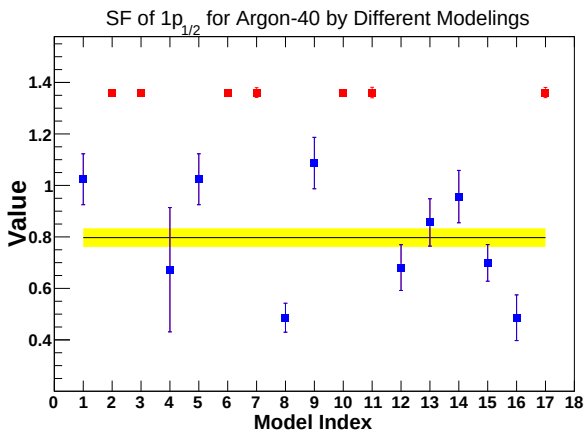
SF of 1p1/2 for Argon-40 by Different Modelings
Value
Model Index

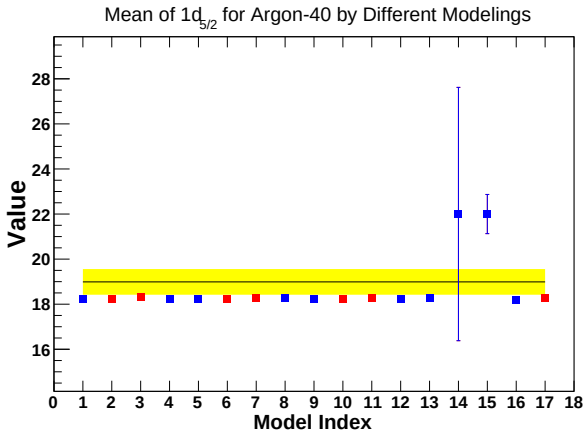
Mean of 1d5/2 for Argon-40 by Different Modelings
Value
Model Index

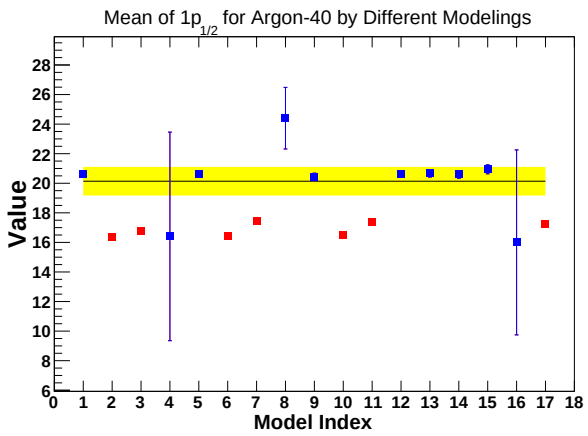
Mean of 1p1/2 for Argon-40 by Different Modelings
Value
Model Index

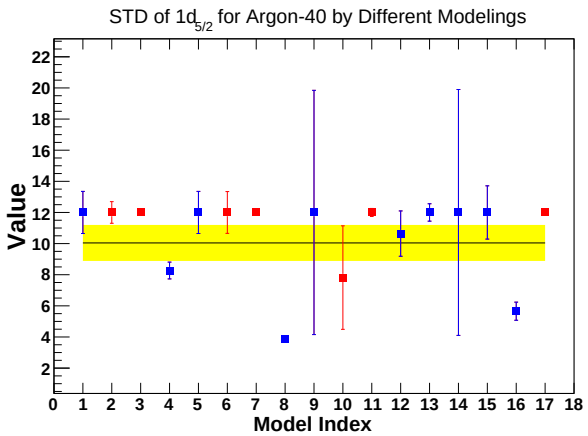
STD of 1d5/2 for Argon-40 by Different Modelings
Value
Model Index

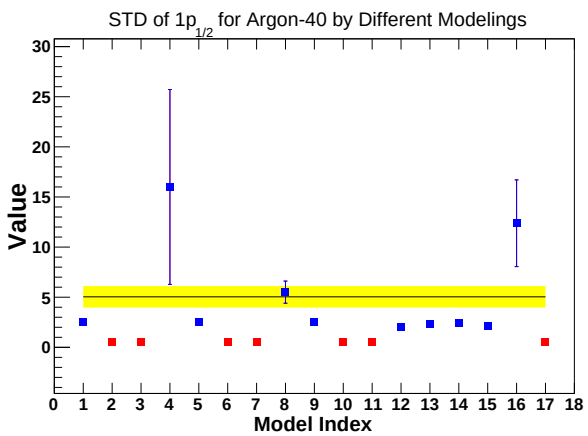
STD of 1p1/2 for Argon-40 by Different Modelings
Value
Model Index

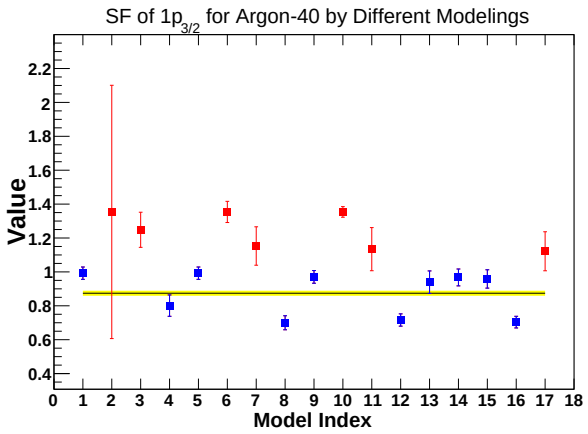
SF of 1p3/2 for Argon-40 by Different Modelings
Value
Model Index

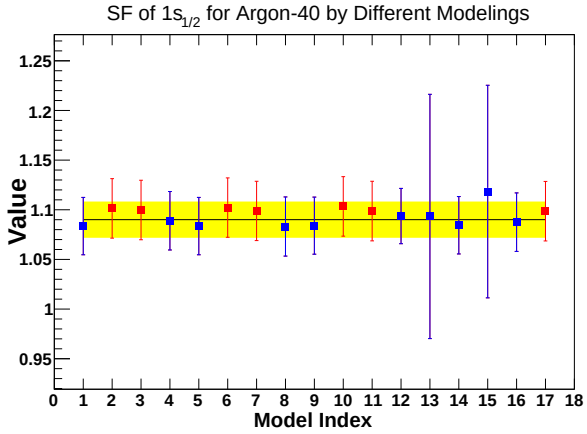
SF of 1s1/2 for Argon-40 by Different Modelings
Value
Model Index

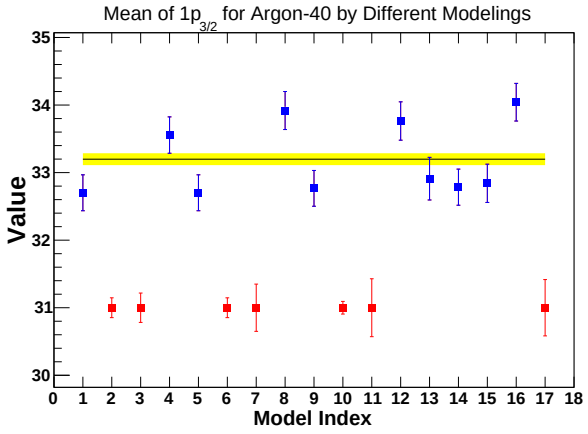
Mean of 1p3/2 for Argon-40 by Different Modelings
Value
Model Index

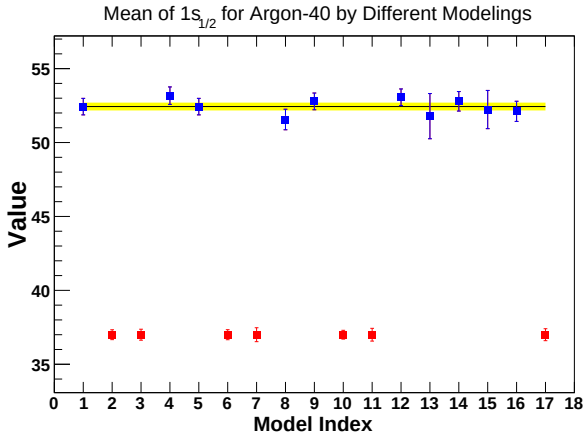
Mean of 1s1/2 for Argon-40 by Different Modelings
Value
Model Index

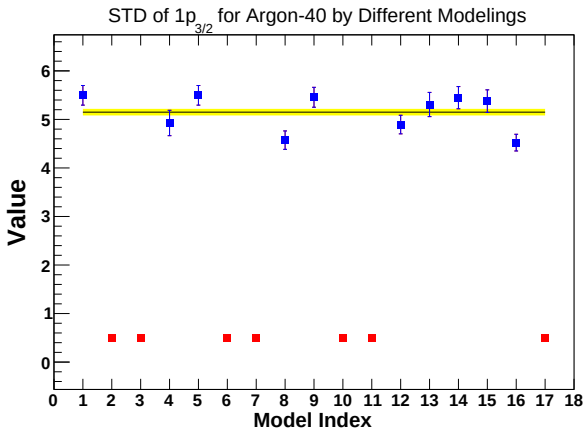
STD of 1p3/2 for Argon-40 by Different Modelings
Value
Model Index

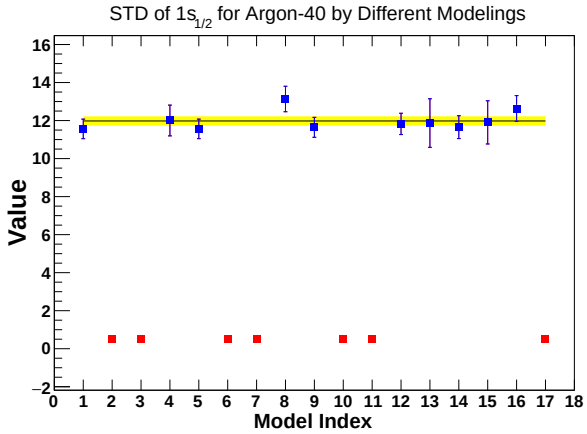
STD of 1s1/2 for Argon-40 by Different Modelings
Value
Model Index

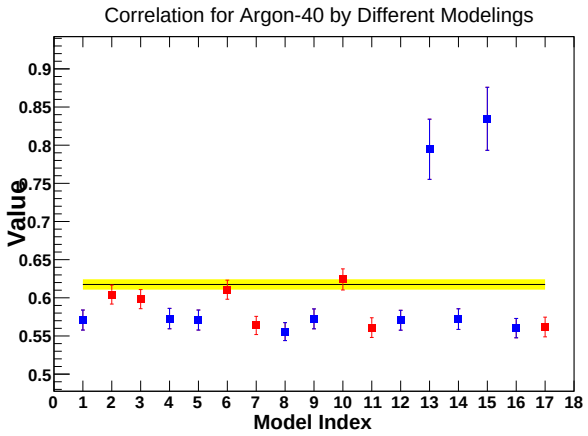
Correlation for Argon-40 by Different Modelings
Value
Model Index

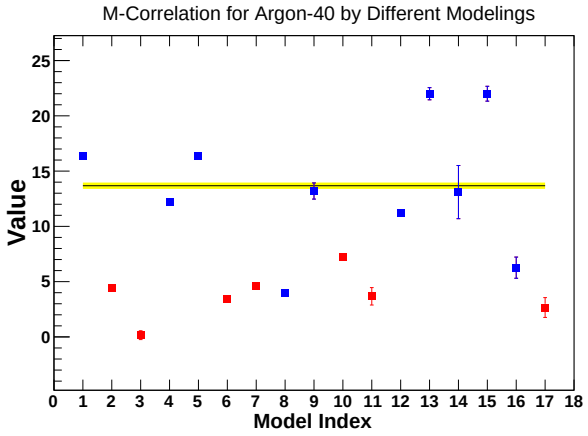
M-Correlation for Argon-40 by Different Modelings
Value
Model Index

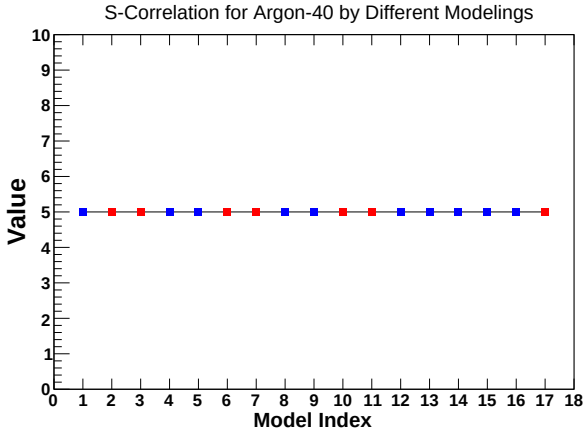
S-Correlation for Argon-40 by Different Modelings
Value
Model Index

TITANIUM

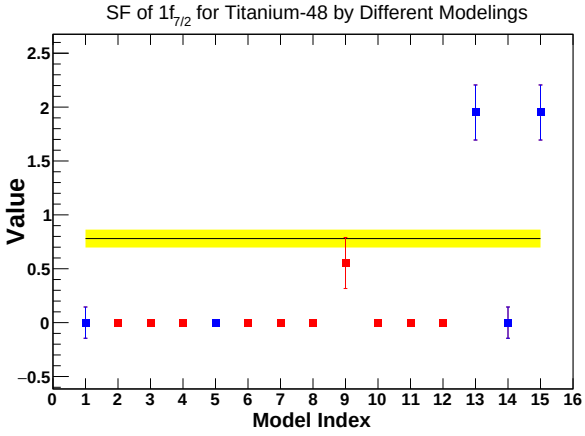
SF of 1f7/2 for Titanium-48 by Different Modelings
Value
Model Index

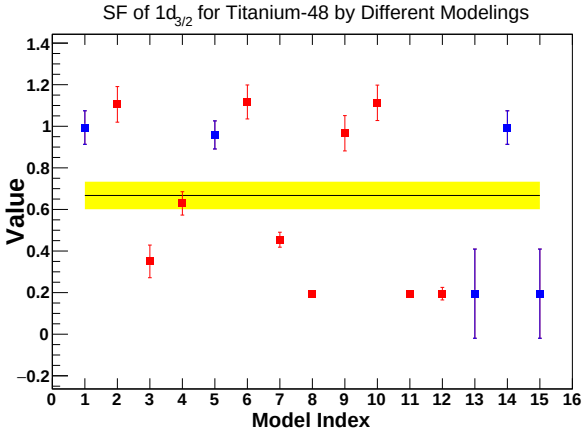
SF of 1d3/2 for Titanium-48 by Different Modelings
Value
Model Index

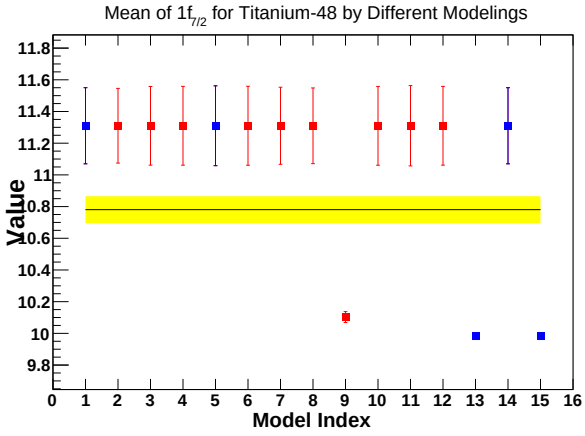
Mean of 1f7/2 for Titanium-48 by Different Modelings
Value
Model Index

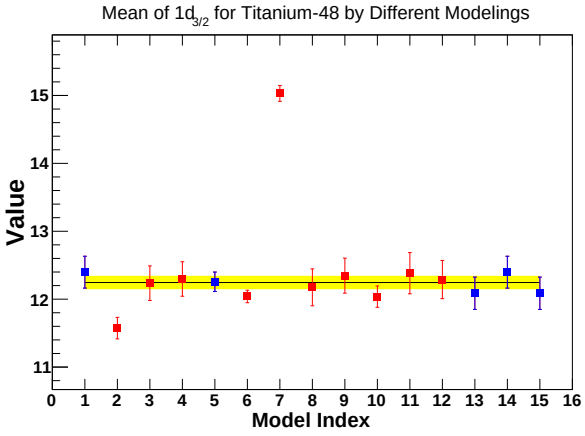
Mean of 1d3/2 for Titanium-48 by Different Modelings
Value
Model Index

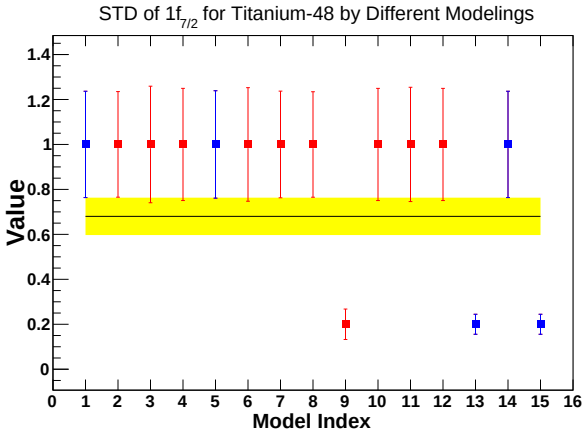
STD of 1f7/2 for Titanium-48 by Different Modelings
Value
Model Index

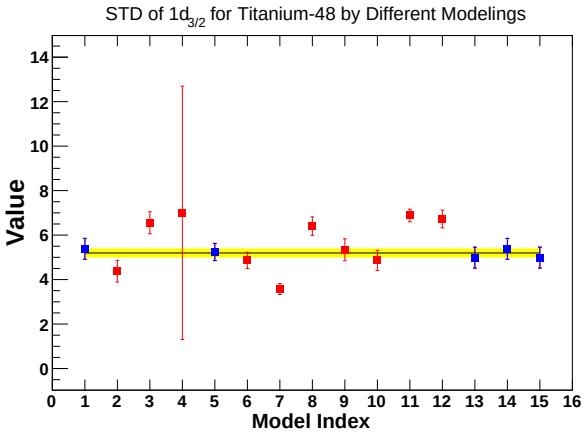
STD of 1d3/2 for Titanium-48 by Different Modelings
Value
Model Index

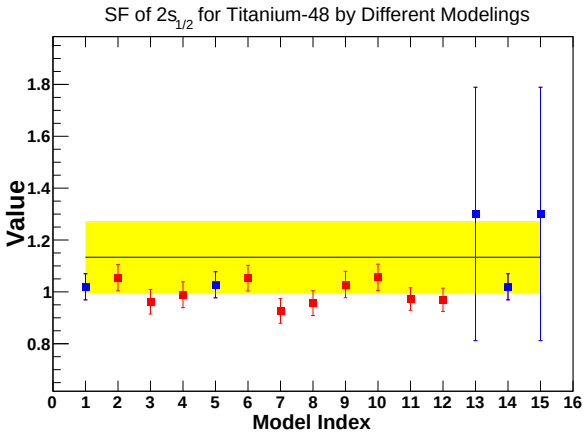
SF of 2s1/2 for Titanium-48 by Different Modelings
Value
Model Index

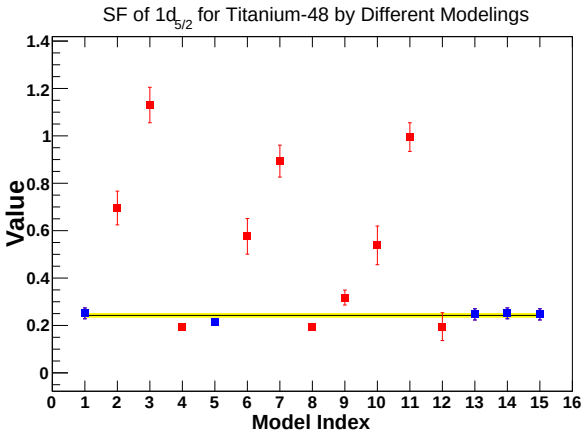
SF of 1d5/2 for Titanium-48 by Different Modelings
Value
Model Index

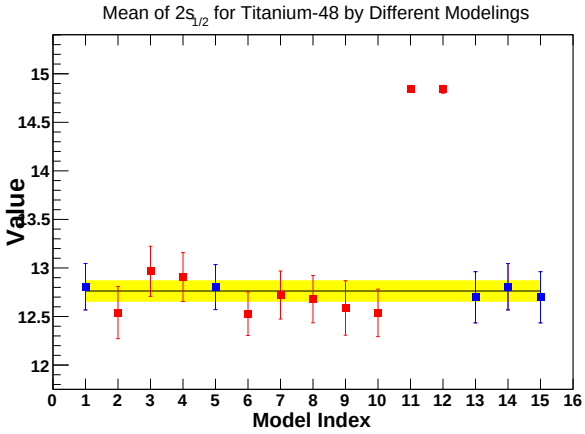
Mean of 2s1/2 for Titanium-48 by Different Modelings
Value
Model Index

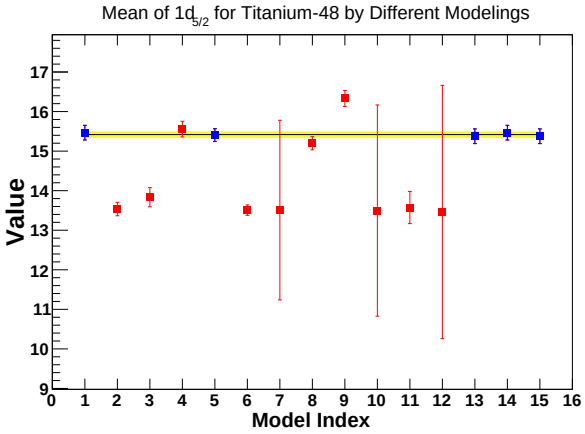
Mean of 1d5/2 for Titanium-48 by Different Modelings
Value
Model Index

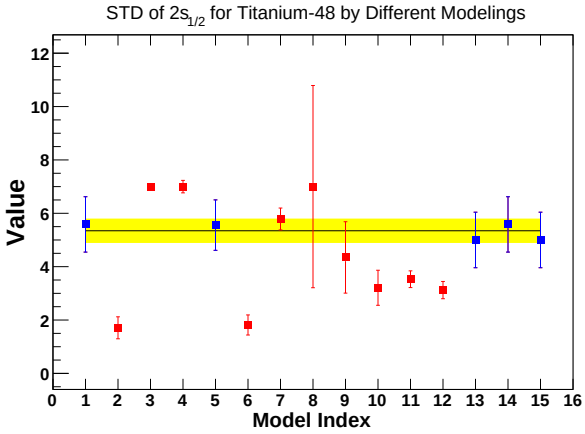
STD of 2s1/2 for Titanium-48 by Different Modelings
Value
Model Index

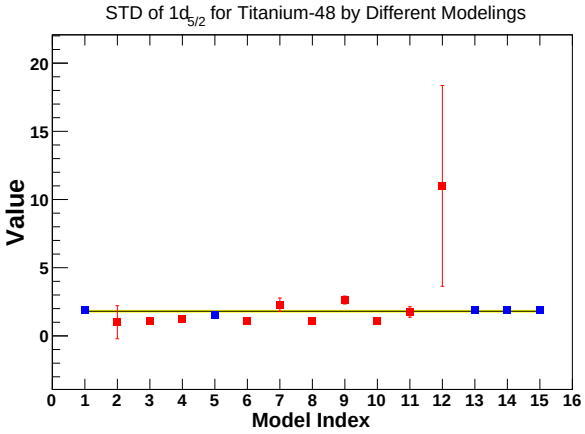
STD of 1d5/2 for Titanium-48 by Different Modelings
Value
Model Index

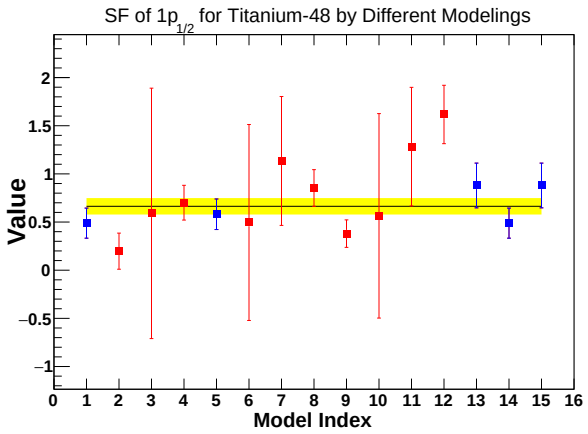
SF of 1p1/2 for Titanium-48 by Different Modelings
Value
Model Index

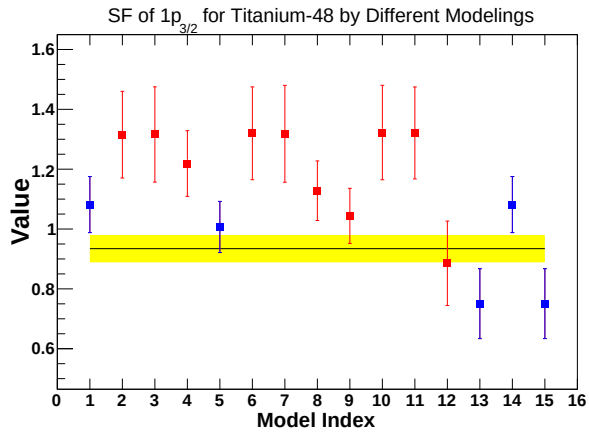
SF of 1p3/2 for Titanium-48 by Different Modelings
Value
Model Index

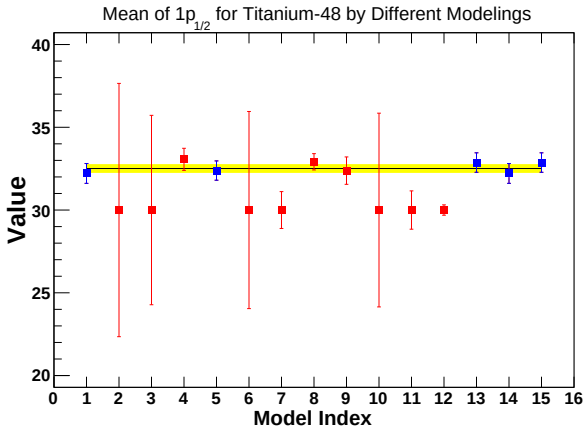
Mean of 1p1/2 for Titanium-48 by Different Modelings
Value
Model Index

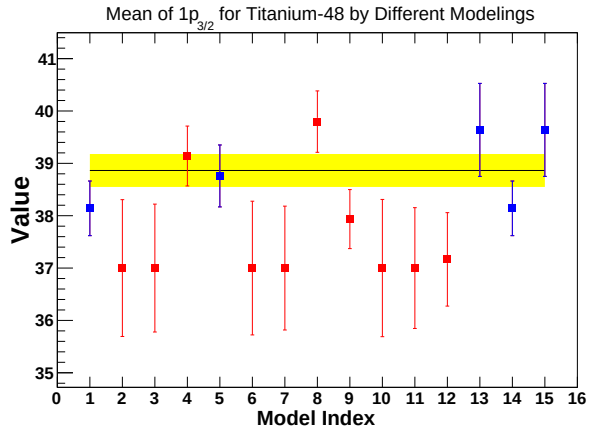
Mean of 1p3/2 for Titanium-48 by Different Modelings
Value
Model Index

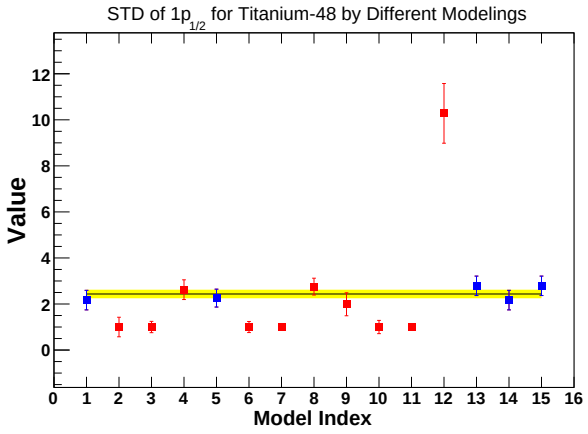
STD of 1p1/2 for Titanium-48 by Different Modelings
Value
Model Index

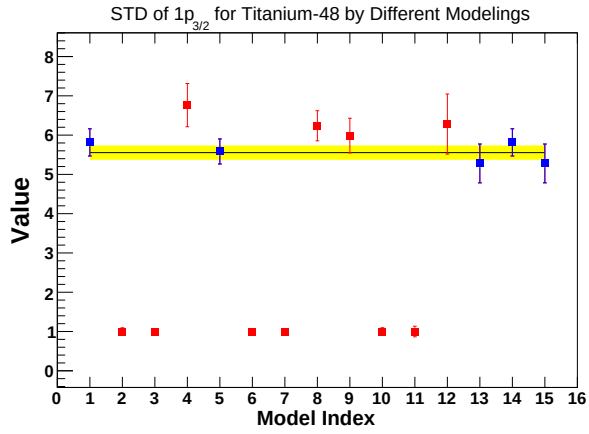
STD of 1p3/2 for Titanium-48 by Different Modelings
Value
Model Index

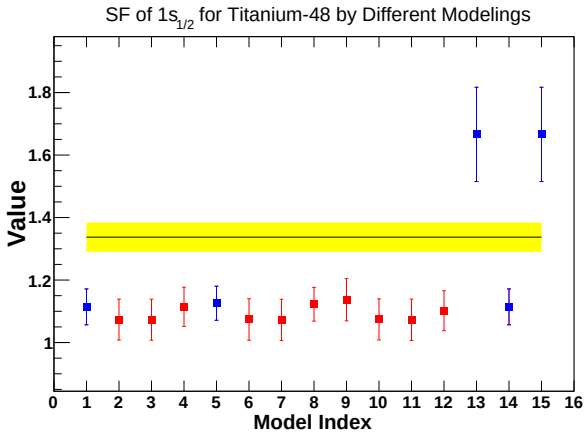
SF of 1s1/2 for Titanium-48 by Different Modelings
Value
Model Index

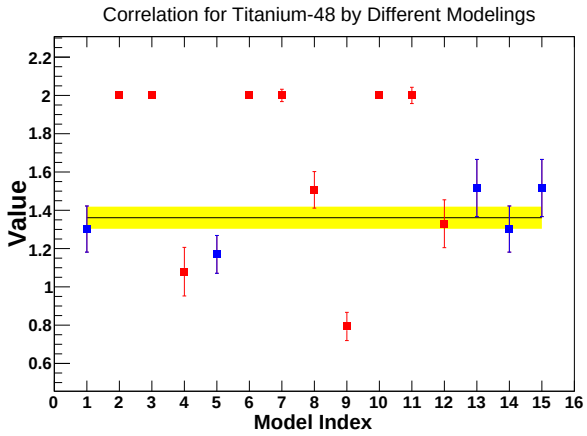
Correlation for Titanium-48 by Different Modelings
Value
Model Index

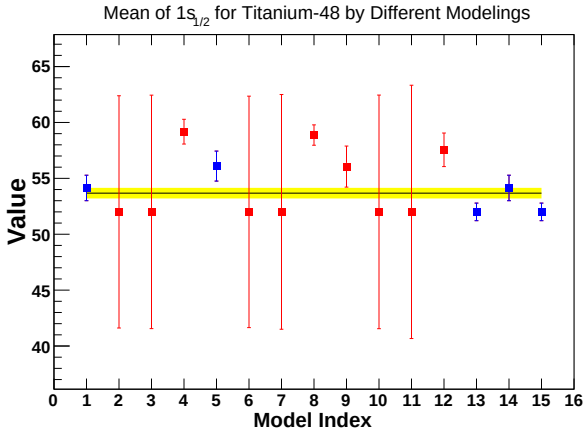
Mean of 1s1/2 for Titanium-48 by Different Modelings
Value
Model Index

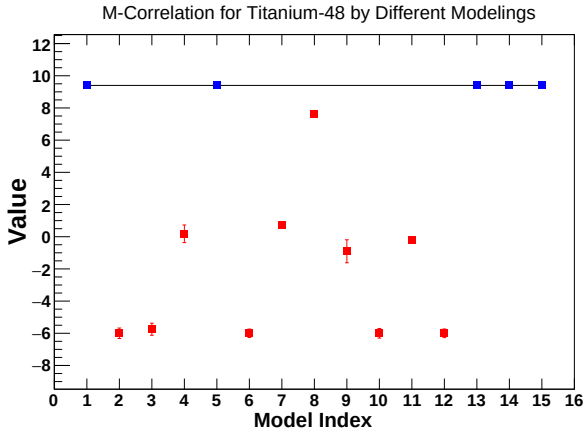
M-Correlation for Titanium-48 by Different Modelings
Value
Model Index

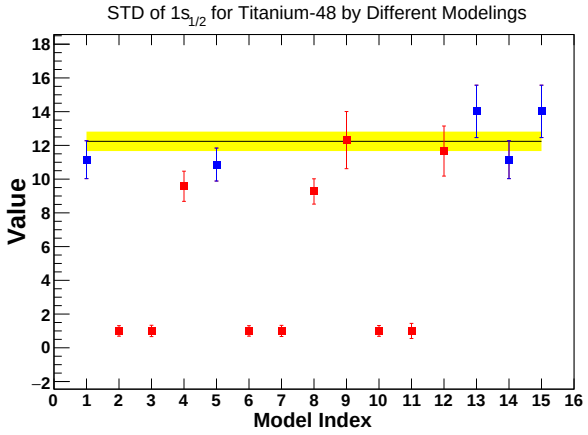
STD of 1s1/2 for Titanium-48 by Different Modelings
Value
Model Index

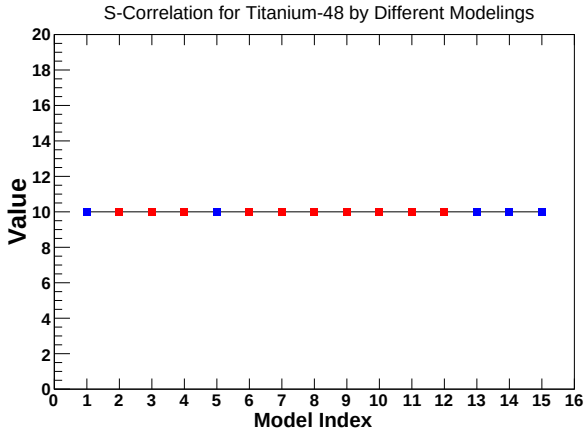
S-Correlation for Titanium-48 by Different Modelings
Value
Model Index